

# Single-crystalline gold nanodisks on WS<sub>2</sub> mono- and multilayers: Strong coupling at room temperature

Mathias Geisler,<sup>†,‡</sup> Ximin Cui,<sup>¶</sup> Jianfang Wang,<sup>¶</sup> Tomas Rindzevicius,<sup>§,||</sup>  
 Lene Gammelgaard,<sup>‡,§</sup> Bjarke S. Jessen,<sup>‡,§</sup> P. A. D. Gonçalves,<sup>†,‡,⊥</sup>  
 Francesco Todisco,<sup>⊥</sup> Peter Bøggild,<sup>‡,§</sup> Anja Boisen,<sup>§,||</sup> Martijn Wubs,<sup>†,‡</sup>  
 N. Asger Mortensen,<sup>‡,⊥,#</sup> Sanshui Xiao,<sup>†,‡</sup> and Nicolas Stenger<sup>\*,†,‡</sup>

<sup>†</sup>*Department of Photonics Engineering, Technical University of Denmark, DK-2800 Kgs. Lyngby, Denmark*

<sup>‡</sup>*Center for Nanostructured Graphene (CNG), Technical University of Denmark, DK-2800 Kgs. Lyngby, Denmark*

<sup>¶</sup>*Department of Physics, The Chinese University of Hong Kong, Shatin, Hong Kong SAR, China*

<sup>§</sup>*Department of Micro- and Nanotechnology, Technical University of Denmark, DK-2800 Kgs. Lyngby, Denmark*

<sup>||</sup>*DNRF and Villum Fonden Center for Intelligent Drug Delivery and Sensing Using Microcontainers and Nanomechanics (IDUN), Technical University of Denmark, DK-2800 Kgs. Lyngby, Denmark*

<sup>⊥</sup>*Center for Nano Optics, University of Southern Denmark, DK-5230 Odense M, Denmark*  
<sup>#</sup>*Danish Institute for Advanced Study, University of Southern Denmark, DK-5230 Odense M, Denmark*

E-mail: niste@fotonik.dtu.dk

## Abstract

Engineering light-matter interactions up to the strong-coupling regime at room temperature is one of the cornerstones of modern nanophotonics. Achieving this goal will enable new platforms for potential applications such as quantum information processing, quantum light sources and even quantum metrology. Materials like transition metal dichalcogenides (TMDC) and in particular tungsten disulfide (WS<sub>2</sub>) possess large transition dipole moments comparable to semiconductor-based quantum dots, and strong exciton binding energies allowing the detailed exploration of light-matter interactions at room temperature. Additionally, recent works have shown that coupling TMDCs

to plasmonic nanocavities with light tightly focused on the nanometer scale can reach the strong-coupling regime at ambient conditions. Here, we use ultra-thin single-crystalline gold nanodisks featuring large in-plane electromagnetic dipole moments aligned with the exciton transition-dipole moments located in monolayer WS<sub>2</sub>. Through scattering and reflection spectroscopy we demonstrate strong coupling at room temperature with a Rabi splitting of  $\sim 108$  meV. In order to go further into the strong-coupling regime and inspired by recent experimental work by Stührenberg et al., we couple these nanodisks to multilayer WS<sub>2</sub>. Due to an increase in the number of excitons coupled to our nanodisks, we achieve a Rabi splitting of  $\sim 175$  meV, a major increase of 62%. To

our knowledge, this is the highest Rabi splitting reported for TMDCs coupled to open plasmonic cavities. Our results suggest that ultrathin single-crystalline gold nanodisks coupled to WS<sub>2</sub> represent an exquisite platform to explore light-matter interactions.

## Keywords

Plasmonics, TMDC, WS<sub>2</sub>, strong coupling, excitons, gold nanodisks

Efficient coupling between light and matter is important for many applications as well as for fundamental research within the field of nanophotonics. When the exchange rate of energy between an emitter and a cavity exceeds their intrinsic dephasing rates, the system enters the strong-coupling regime where new hybrid eigenstates form that are part light and part matter.<sup>1</sup> Reaching the strong-coupling limit in different systems has among others allowed for the study of quantum electrodynamics,<sup>2</sup> experimental realization of low-threshold lasers,<sup>3</sup> and for coupling a single quantum of energy to nitrogen-vacancy centers in diamond.<sup>4,5</sup> However, these investigations all required low temperatures as the emitter dephasing occurs too rapidly or the energy dissipation is too high at ambient conditions.

The transition into the strong-coupling regime is dependent on the ability to control the electromagnetic coupling rate  $g$  between the emitter and the cavity. Since  $g \propto \mu_{\text{ex}} \sqrt{N/V}$ ,<sup>6</sup> where  $\mu_{\text{ex}}$  is the transition-dipole moment of the emitter,  $N$  is the number of excitons coherently coupled to the cavity, and  $V$  is the cavity mode volume, several key factors can be engineered to facilitate this transition. For purely dielectric cavities, the minimum mode volume is on the order of  $(\lambda/n)^3$ , thereby limiting the coupling strength achievable and requiring long coherence times in the cavity and emitter states to observe the strong-coupling regime. On the other hand, plasmonics offers the possibility for a significant reduction in the mode volume due to the sub-diffraction confinement of the electric field and the associated strong enhancement of the field strength at the price of

higher losses, mainly due to absorption in the metal.<sup>7</sup> Utilizing this to couple plasmons to various organic and inorganic semiconductors has gained increasing attention in recent years,<sup>8–13</sup> and plasmonic systems have been shown to reach the strong-coupling regime when interacting with organic molecules,<sup>6,14–17</sup> resulting in enhanced nonlinearities and low threshold polariton lasing and condensation.<sup>18,19</sup>

Regarding excitons in two-dimensional (2D) materials, mono- and multilayers of TMDCs have been the object of intense study in recent years in part due to their unique optical properties, capable of merging together the main properties of Frenkel excitons in organic semiconductors (high binding energy and large oscillator strength) with that of Wannier–Mott excitons in inorganic quantum wells (relatively large exciton radius, low photodegradation and small saturation density) at room temperature. However, the exciton-dipole moment is strongly oriented in the plane of the 2D material,<sup>10</sup> which requires special attention when coupling to external fields. Overcoming this challenge has resulted in studies demonstrating strong coupling of the excitons in 2D materials to plasmonic lattices,<sup>20,21</sup> plasmonic and dielectric cavities,<sup>22–27</sup> plasmonic slit resonators,<sup>28</sup> as well as to individual plasmonic nanoparticles.<sup>29,30</sup> Some studies have even reported strong coupling to charged excitons (trions) in WS<sub>2</sub>,<sup>31</sup> and self-hybridization of the exciton with cavity modes in extended TMDC systems.<sup>32–34</sup> The lattice structure of the TMDCs furthermore gives rise to a new degree of freedom in the form of valley polarization, which can be addressed using circularly polarized light when coupled to plasmonic structures.<sup>35,36</sup>

In this work we present the observation of the strong-coupling regime between localized surface plasmons supported by chemically synthesized, single-crystalline gold nanodisks, and 2D excitons in mono- and multilayer WS<sub>2</sub>. Both systems exhibit strong in-plane optical response, and by careful control of the nanoparticles' size and position we achieve spectral and spatial overlap between the dipolar plasmon mode in the nanodisks and the A-exciton in WS<sub>2</sub>.<sup>37,38</sup> Since the nanodisks are sufficiently

thin, the absorption dominates the extinction cross section, and we are therefore able to experimentally observe the onset of the strong-coupling regime in both scattering and reflection measurements with a Rabi splitting of  $108 \pm 8$  meV at room temperature. Inspired by recent findings,<sup>30</sup> we furthermore present results obtained from multilayer  $\text{WS}_2$  resulting in strong coupling with a Rabi splitting of  $175 \pm 9$  meV. To the best of our knowledge, this is the highest reported splitting in any TMDC coupled to an open plasmonic cavity. The accessibility of the cavity along with the clear presence of the strong-coupling regime is an important stepping stone towards further study of the plethora of fundamental physics in these strongly coupled light-matter systems, along with potential applications in quantum information processing, quantum metrology, nonlinear optical materials, and quantum light sources.

## Results and discussion

In order to demonstrate the strong-coupling regime at room temperature, we deposit thin single-crystalline gold nanodisks on a monolayer of  $\text{WS}_2$  as shown in Figure 1a. The nanodisks were chosen for their strong in-plane, dipolar localized surface-plasmon resonances (LSPR) with narrow linewidths which are tunable by controlling their radius.<sup>37</sup> Like the other TMDCs,  $\text{WS}_2$  has a strong in-plane excitonic response with a large transition-dipole moment.<sup>10,39</sup> Combined with the stability of the excitons under ambient conditions due to their large binding energies,<sup>40</sup> this makes  $\text{WS}_2$  highly suitable for exploring light-matter coupling at room temperature.

Flakes of  $\text{WS}_2$  were mechanically exfoliated from commercially available crystals (HQ Graphene) onto plasma cleaned  $\text{SiO}_2/\text{Si}$  substrates. Monolayer flakes were automatically detected and identified by quantitative optical mapping.<sup>41</sup> The monolayer nature of these flakes was confirmed by atomic force microscopy (AFM) as depicted in Figure 1b, where the height of the flake was found to be

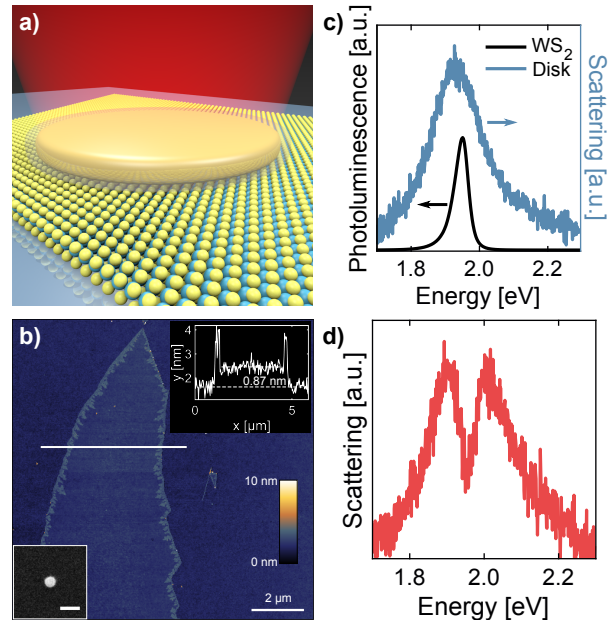


Figure 1: **(a)** Sketch of a single-crystalline gold nanodisk coupled to monolayer  $\text{WS}_2$ . **(b)** Atomic force microscopy image of the monolayer  $\text{WS}_2$  flake. The inset in the lower left corner shows a scanning electron microscopy image of a typical nanodisk. Scale bar is 100 nm. **(c)** Photoluminescence spectrum of monolayer  $\text{WS}_2$  (black) and dark-field scattering spectrum of an individual, uncoupled nanodisk (blue). **(d)** Experimental scattering spectrum of a single nanodisk coupled to  $\text{WS}_2$  clearly showing the splitting between the upper and lower polariton branch.

0.87 nm in agreement with previously reported results.<sup>38</sup> The photoluminescence (PL) spectrum, black line in Figure 1c, reveals the exciton emission spectrum, where the asymmetry of the peak to the low-energy side is mainly caused by strong exciton-phonon coupling,<sup>42</sup> and also indicates the presence of the trion (charged exciton) in addition to the neutral state of the A-exciton.<sup>43</sup> Fitting a double Voigt profile to the PL spectrum yields emission energies of  $E_{\text{em,tri}} = 1.922$  eV and  $E_{\text{em,ex}} = 1.951$  eV, in accordance with the literature<sup>38</sup> (see Figure S1). To extract the energy and linewidth of the A-exciton resonance, we performed reflection measurements on five different monolayer flakes, using spatially filtered white light to ensure normal incidence. Employing the transfer-matrix method<sup>44</sup> we obtained the dielectric function  $\varepsilon$  for the flakes from which we extract an average exciton energy  $E_{\text{ex}} = 1.963$  eV and linewidth  $\gamma_{\text{ex}} = 28$  meV, see Figure S3 and Table S1.

The open plasmonic cavities consist of circular single-crystalline gold nanodisks chemically synthesized as described previously.<sup>37</sup> Briefly, triangular gold nanoplates were first synthesized using a three-step seed-mediated method.<sup>45</sup> The nanodisks were produced by performing anisotropic oxidation on the nanoplates. The oxidation allows for finely tailoring the nanodisk diameter, and the thickness of the gold nanodisks remained unchanged during the oxidation process. A thin layer ( $\sim 1$  nm) of cetyltrimethylammonium bromide (CTAB) is present on the surface of the nanodisks after the synthesis.<sup>37</sup> In our study, circular gold nanodisks of  $8.8 \pm 0.2$  nm in thickness, measured without the CTAB layer, were chosen because of their moderate plasmon damping and concomitant narrow plasmon linewidth. Due to the inherent variation in particle radii, each batch contains particles with their LSPR distributed around a mean energy, the latter chosen to match the exciton energy ( $E_{\text{ex}} = 1.963$  eV). A representative scattering spectrum of a single gold nanodisk is shown in Figure 1c. Measuring the uncoupled nanodisks on the bare  $\text{SiO}_2/\text{Si}$  substrate results in an average linewidth of the plasmon resonance of  $\gamma_{\text{pl}} = 170$  meV. The variation of the particles' LSPRs is exempli-

fied in ensemble measurements performed on the nanodisk solution in Figure S2, where the extinction spectra show a width about twice that of the individual nanodisks due to inhomogeneous broadening. With an energy of the resonance around 1.96 eV we obtain a  $Q$ -factor of  $E_{\text{pl}}/\gamma_{\text{pl}} \approx 11.5$  close to its intrinsic quasistatic limit of  $\sim 13.5$  for an arbitrarily shaped gold nanoparticle when only the dielectric function is considered.<sup>46</sup> This shows that other dissipation pathways, such as surface and imperfection scattering, are minimized due to the single-crystalline nature of the nanodisks.

Achieving the strong electromagnetic coupling requires simultaneous spatial and spectral overlap of the LSPR and the exciton in the nanodisk and  $\text{WS}_2$ , respectively. The spatial overlap was ensured by dropcasting the nanodisks directly onto the  $\text{WS}_2$  flakes. The CTAB molecule layer ensures a narrow gap without direct contact between the metal and the underlying flake in order to prevent possible quenching. The presence of a high refractive-index material under the particle furthermore serves to concentrate the electric field in the  $\text{WS}_2$  and in the substrate rather than in the surrounding air. Spectral overlap was achieved by precise control of the nanodisk radius. We took advantage of the aforementioned natural variation of the nanodisk radii inherent in a batch, as this allowed for measurements on different gold nanodisks with their plasmon energies distributed around the energy of the exciton. The positions of the particles were then examined by dark-field (DF) microscopy, and scattering spectra were obtained for each individual particle. After the measurements, scanning electron microscope images were taken to ensure the measured spectra originate only from single nanodisks rather than from dimers or individual particles of more complex shape. A spectrum taken from a nanoparticle resting on a  $\text{WS}_2$  monolayer is shown in Figure 1d, where two distinct peaks appear around the bare exciton energy. The almost equal strength of the two peaks indicates that the LSPR of the nanodisk is close to the exciton resonance. By measuring particles with different radii, and thus different LSPR energies, we are in this manner

able to map out the dispersion of the coupled system as a function of the plasmon-exciton energy detuning. All the examined spectra show a double peaked lineshape. Extracting the energy of the peaks from the scattering spectra, a clear anti-crossing behaviour is observed as shown in Figure 2a, which is characteristic for these emitter-cavity coupled systems.<sup>1,16,17</sup>

In order to analyze the data, we apply the coupled-oscillator model in its non-Hermitian Hamiltonian form given by the eigenvalue problem:<sup>47</sup>

$$\begin{bmatrix} E_{\text{pl}} - i\frac{\gamma_{\text{pl}}}{2} & g \\ g & E_{\text{ex}} - i\frac{\gamma_{\text{ex}}}{2} \end{bmatrix} \begin{bmatrix} \alpha \\ \beta \end{bmatrix}_{\pm} = E_{\pm} \begin{bmatrix} \alpha \\ \beta \end{bmatrix}_{\pm}, \quad (1)$$

where  $E_{\text{pl}}$  and  $\gamma_{\text{pl}}$  are the plasmon energy and linewidth,  $E_{\text{ex}}$  and  $\gamma_{\text{ex}}$  are the exciton energy and linewidth,  $g$  is the coupling strength, and  $\alpha$  and  $\beta$  are the Hopfield coefficients describing the polaritonic state in terms of its plasmonic ( $\alpha_{\pm}$ ) and excitonic ( $\beta_{\pm}$ ) constituents. Diagonalizing the Hamiltonian yields the two energy eigenvalues

$$E_{\pm} = \frac{1}{2}(E_{\text{pl}} + E_{\text{ex}}) - \frac{i}{4}(\gamma_{\text{pl}} + \gamma_{\text{ex}}) \pm \sqrt{g^2 + \frac{1}{4}\left(\delta - \frac{i}{2}(\gamma_{\text{pl}} - \gamma_{\text{ex}})\right)^2}, \quad (2)$$

where we have introduced the detuning  $\delta = E_{\text{pl}} - E_{\text{ex}}$  of the plasmon with respect to the exciton energy. The eigenvalues describe an energy spectrum divided into the upper polariton branch (UPB,  $E_{+}$ ) and the lower polariton branch (LPB,  $E_{-}$ ). The vacuum Rabi splitting  $E_{\text{Rabi}}$  is then defined as the energy difference between the UPB and LPB exactly at zero detuning, giving

$$E_{\text{Rabi}} = \sqrt{4g^2 - \frac{(\gamma_{\text{pl}} - \gamma_{\text{ex}})^2}{4}}. \quad (3)$$

From the scattering spectra of the individual nanodisks on  $\text{WS}_2$  we read off the respective energies of the upper and lower polariton branches,  $E_{+}$  and  $E_{-}$ . From energy conservation we then obtain the plasmon energy as  $E_{\text{pl}} = E_{+} + E_{-} - E_{\text{ex}}$ . The avoided crossing

appears clearly on the histogram in the right side of Figure 2a, with no data points located between the two polaritonic branches. The vertical error bars account for a read-off uncertainty of the energies  $E_{\pm}$  which we estimate to be  $\pm 5$  meV. The horizontal error bars represent the propagated uncertainties in the calculated detunings, which are dominated by the standard deviation of the measured exciton energy.

To estimate the coupling strength  $g$  and the vacuum Rabi splitting  $E_{\text{Rabi}}$ , we simultaneously fit the real part of the eigenvalue spectrum Equation 2 to the experimentally determined dispersion of the UPB and LPB. In the fitting procedure we fix the values of the exciton energy, ( $E_{\text{ex}} = 1.963$  eV), the exciton linewidth ( $\gamma_{\text{ex}} = 28$  meV), and the plasmon linewidth ( $\gamma_{\text{pl}} = 170$  meV) to the experimentally determined values, which leaves the coupling strength as the only free parameter. This procedure yields a value of  $g = 64 \pm 3$  meV, from which we calculate a Rabi splitting of  $E_{\text{Rabi}} = 108 \pm 8$  meV using Equation 3. Comparing this with the overall losses in the system  $\frac{1}{2}(\gamma_{\text{pl}} + \gamma_{\text{ex}}) = 99 \pm 3$  meV, we see that our hybrid nanodisk/ $\text{WS}_2$  system is at the onset of the strong-coupling regime since as per the criterion  $E_{\text{Rabi}} > \frac{1}{2}(\gamma_{\text{pl}} + \gamma_{\text{ex}})$ .

Five scattering spectra showing the evolution of the optical response of the hybrid system are depicted in Figure 2b. Here we clearly see the avoided crossing in the succession of individual spectra, where the scattering amplitude is shifting from the LPB to the UPB as the detuning is scanned across the direct energy match between plasmon and exciton at  $\delta = 0$  meV. In addition, we note that the noise generally increases for larger  $\delta$  since the LSPR resonance energy increases with decreasing particle radius, resulting in a lower scattering cross section.

Since  $\delta = E_{+} + E_{-} - 2E_{\text{ex}}$ , the exact value for the detuning reported in Figure 2b-c is highly sensitive to the value of  $E_{\text{ex}}$ . From reflection measurements we observe exciton energies in the range 1.958 eV to 1.968 eV, that can result as a consequence of local strain or doping from the nanoparticle solution during deposition. Extracting the exciton energy from the fitting with the coupled oscillator model we ob-

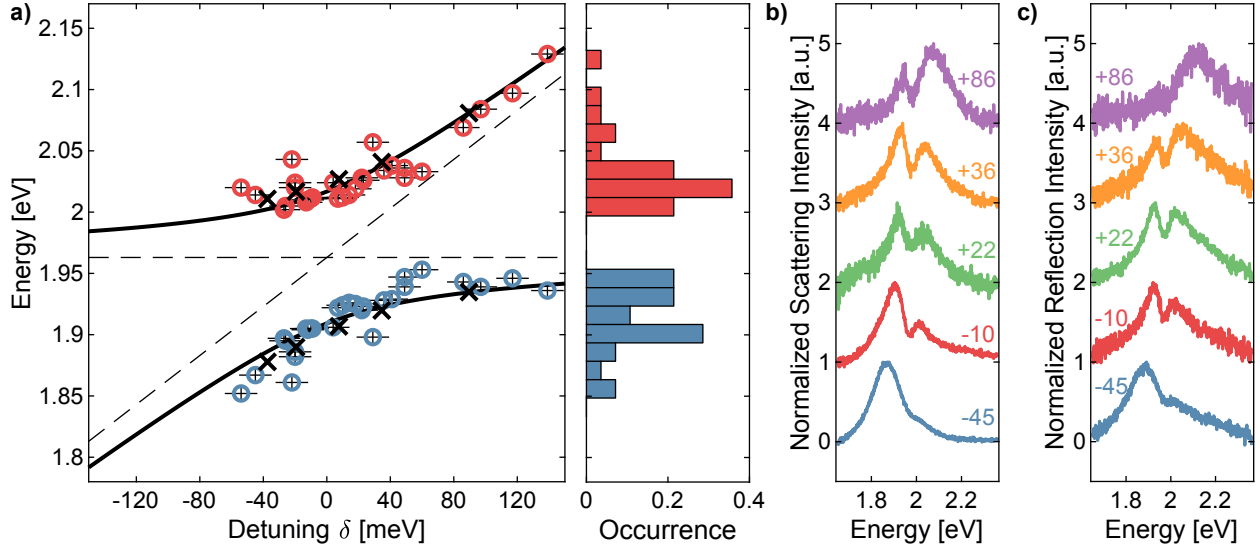


Figure 2: **(a)** Experimental dispersion obtained from scattering measurements for the coupled plasmon-exciton system on monolayer  $\text{WS}_2$  with the lower (blue) and upper (red) polariton branch. The right panel shows the distribution of measured peaks. The solid black line is a fit to the data using Equation 2, while the horizontal and sloped dashed lines indicate the exciton and plasmon energies, respectively. The black crosses are the peak positions extracted from the calculated spectra shown in Figure 3b. **(b)** Experimental dark-field scattering spectra from five different single gold nanodisks showing the evolution of the optical response with different plasmon energies. The individual detunings  $\delta = E_{\text{pl}} - E_{\text{ex}}$  are presented next to the spectra. **(c)** Experimental reflection spectra for the same five particles as in **(b)**. The absorption of the disks dominates the extinction spectra by approximately an order of magnitude making the reflection spectrum representative of the particle absorption (see Figure 3a).

tain a slightly higher value ( $E_{\text{ex}}=1.981\pm 0.04$  eV, see Figure S5) that fits within the statistical error from the fitting procedure and does not affect the evaluated Rabi splitting (see Figure S6).

Since  $\delta = E_+ + E_- - 2E_{\text{ex}}$ , the exact value for  $\delta$  reported in Figure 2b-c is highly sensitive to the value of  $E_{\text{ex}}$ . From the reflection measurements we observe exciton energies in the range 1.958 eV to 1.968 eV giving a detuning variation of  $\Delta\delta = 20$  meV, which could be expected to influence the resulting fit as well. To validate our results, we therefore also use the coupled-oscillator model to extract the peak positions of the UPB and LPB, and to obtain the exciton energy,<sup>48</sup> see Figure S4. From this we find a slightly higher exciton energy of  $E_{\text{ex}} = 1.981$  eV, but also a larger spread of 40 meV (i.e.  $\Delta\delta = 80$  meV). This larger variation and change in  $E_{\text{ex}}$  can be caused by e.g. local strain or doping from the nanoparticle solution.<sup>49</sup> However, using instead this average in the same analysis as before results in a change in the Rabi splitting of only 4 meV, despite the shift of 36 meV in the detuning for all measurement points, see Figure S5. In any case we can conclude from this analysis that our system is at the onset of the strong-coupling regime whether we use one or the other of the above methods to determine  $E_{\text{ex}}$ .

The strong-coupling regime is associated with a pronounced mode splitting not only in the scattering but also in the absorption spectrum of the coupled system.<sup>50</sup> Usually, the presence of this splitting in absorption is only verified numerically,<sup>29,30</sup> since measuring the absorption independently from the scattering normally requires specialized techniques.<sup>51</sup> However, as our nanodisks have small radii ( $< 35$  nm) and a thickness of only 8.8 nm, our numerical calculations show that the absorption cross section is larger than the scattering cross section by more than an order of magnitude, as depicted in Figure 3a, and thus dominates the reflection spectrum entirely. By measuring the reflection spectra of the particles, we therefore have direct access to the absorption spectrum and through that experimental verification of the coupling regime. In Figure 2c the normalized reflection

spectra  $\Delta\mathcal{R}$  of the same five particles as in Figure 2b are shown. The spectrum has been calculated as

$$\Delta\mathcal{R} = \frac{\mathcal{R}_{\text{WS}_2} - \mathcal{R}_{\text{disk}}}{\mathcal{R}_{\text{sub}}}, \quad (4)$$

where  $\mathcal{R}_{\text{WS}_2}$ ,  $\mathcal{R}_{\text{disk}}$ , and  $\mathcal{R}_{\text{sub}}$  are the light intensities reflected from the WS<sub>2</sub>, from the nanodisk on the WS<sub>2</sub>, and from the bare SiO<sub>2</sub>/Si substrate, respectively. As  $E_{\text{pl}}$  is tuned across the exciton energy, we observe the same behaviour for the reflection as for the scattering spectra, but we note that the particle absorption is blueshifted in all cases compared to the scattering, which is also observed in our calculations, see Figure 3b-c. This shift is predicted from Mie theory and has also been demonstrated experimentally.<sup>51</sup> The measured mode splitting also in the reflection spectra corroborates the observation of the onset of the strong-coupling regime in our system.

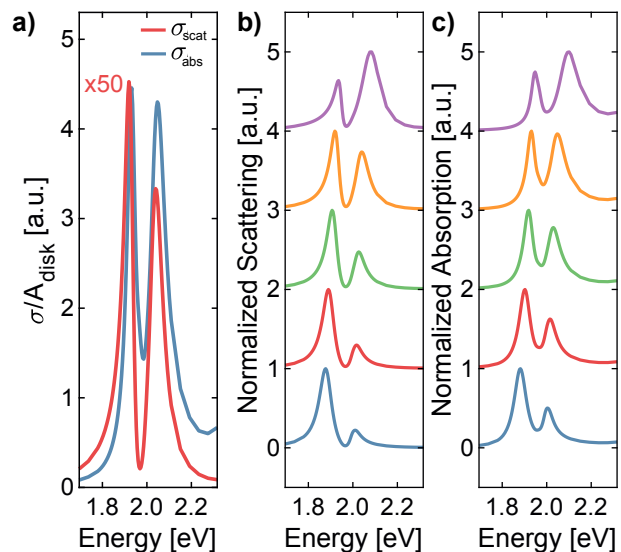


Figure 3: **(a)** Calculated scattering (red) and absorption (blue) cross sections  $\sigma$  obtained with finite-element method calculations of a nanodisk of radius  $R = 23$  nm normalized to the geometrical area. The scattering cross section has been multiplied by 50 to fit the scale. The ratios between the maxima of  $\sigma_{\text{abs}}$  and  $\sigma_{\text{scat}}$  vary from 83 ( $R = 19$  nm) down to 17 ( $R = 29$  nm). **(b-c)** Normalized scattering and absorption of particles of radii  $R = 19$  nm, 23 nm, 25 nm, 27 nm, and 29 nm, arranged from top to bottom.



To further support the experimental observations, we perform finite-element method (FEM) calculations of the electrostatics (see methods part). We use the experimentally determined radii (from 19 nm to 29 nm)<sup>37</sup> and nanodisk thickness (9 nm), as well as a 1 nm thick polymer layer surrounding the particle. We furthermore use our experimentally determined dielectric function of the WS<sub>2</sub> flakes. For the gold, we use the values for  $\epsilon$  measured by McPeak et al.<sup>52</sup> in optimized film quality conditions. This choice of reference data was made to better reflect the single-crystalline nature of our nanoparticles. In this way, we obtain scattering and absorption spectra of the particles as shown in Figure 3b and c. Since the nanodisks are thinner than the skin depth of gold of around 25 nm at 1.96 eV,<sup>53</sup> the electric field completely permeates the particles, making the results very sensitive to the particular value of the dielectric function. For instance, using instead the values from Johnson and Christy<sup>54</sup> redshifts the resonance position by around 40 meV (see Figure S6), and changes in especially the imaginary part of  $\epsilon$  have been reported for thin gold films.<sup>55</sup> However, we still see that we are able to reproduce the experimentally observed behaviour both in scattering and absorption with good agreement, which further corroborates the observation of the onset of the strong-coupling regime in our system. The calculations show cross sections approaching zero at the exciton energy, indicative of strong plasmon-exciton coupling.<sup>50</sup> These same near-zero intensities are not observed in the experiments, which can be caused by a signal background coming from the strong scattering of the WS<sub>2</sub> flake edges. Although we perform background removal on all measured spectra, the scattering cross section of the nanodisks is small and any remaining background is expected to influence the overall signal intensity.

Extracting the peak locations of the calculations in the same manner as for the experimental data allows us to compare the position of the UPB and LPB to the experimental results, as indicated by the black crosses in Figure 2a, where we see excellent agreement between experiments and calculations.

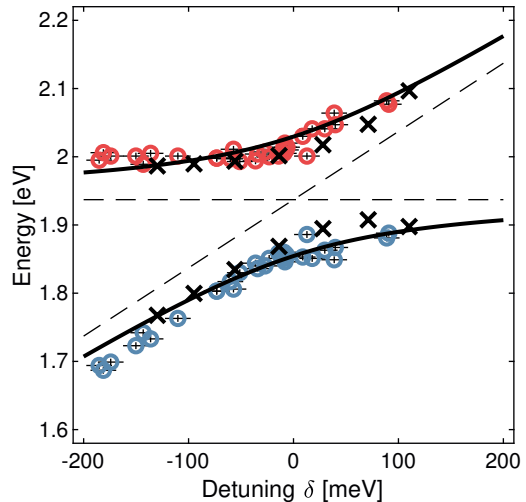


Figure 4: Experimentally obtained dispersion for the coupled plasmon-exciton system on multilayer WS<sub>2</sub>. Note the change in scale of the  $y$ -axis compared to Figure 2a.

Encouraged by the observation of strong coupling of nanodisks on a monolayer, we then went on to study how these gold disks coupled to WS<sub>2</sub> multilayers. Earlier experiments by Kleemann et al.<sup>25</sup> and by Stührenberg et al.<sup>30</sup> have shown the possibility to increase the Rabi splitting by increasing the number of TMDC layers coupled to the plasmonic particle. In the former case the effect comes from a higher out-of-plane excitonic dipole moment in a particle on a mirror cavity, while in the latter case the increase is caused both by a lowering of the mode volume and an increase in the total mode overlap with the excitonic material. A significant increase in the Rabi splitting of  $\sim 22\%$  was observed by Stührenberg and coworkers when going from one to four layers of WSe<sub>2</sub>, after which the effect saturates. In order to assess the magnitude of this effect in our system, we measure the optical response of particles on a WS<sub>2</sub> flake 4.4 nm in height corresponding to seven layers. Using the transfer-matrix method again allows us to extract the dielectric function, giving  $E_{\text{ex,multi}} = 1.942$  eV and  $\gamma_{\text{ex,multi}} = 44$  meV (see Table S2), where both the broadening and redshift of the A-exciton resonance are known phenomena for multilayers.<sup>30</sup> Following the same procedure for data analysis as for the monolayer, we obtain the



experimental results plotted in Figure 4, where we again see the avoided crossing characteristic for these systems. In accordance with the previous results, we also find an increase in the coupling strength to  $g_{\text{multi}} = 93 \pm 4 \text{ meV}$  (an increase of 45%), resulting in a Rabi splitting of  $E_{\text{Rabi,multi}} = 175 \pm 9 \text{ meV}$  (increased by 62%). To the best of our knowledge, this is the highest Rabi splitting reported in a TMDC coupled to an open plasmonic cavity.<sup>26,29,30,56</sup> Even larger splittings can be obtained using the 2D material itself as both emitter host and cavity,<sup>32-34</sup> or by coupling TMDCs to both cavity and localized plasmon modes simultaneously.<sup>57</sup> However, the direct availability of the open plasmonic cavity is advantageous for future near-field explorations and sensing applications, as well external coupling to other cavities and optical circuit elements.

In order to understand the important increase in the coupling strength that we observe for the seven-layer  $\text{WS}_2$  flake, we perform numerical calculations using the dielectric function extracted from our reflection measurements. We again extract the position of the UPB and LPB as shown by the black crosses in Figure 4. The calculations predict an overall increase of the coupling strength with the number of layers. However, quantitatively we observe a slightly lower increase in the Rabi splitting in comparison to our experimental data. We ascribe this difference to the fact that we have approximated the optical response of multilayer  $\text{WS}_2$  as an isotropic dielectric function and we therefore do not take into account the out-of-plane response of multilayer  $\text{WS}_2$ . Despite these quantitative differences we observe qualitative agreement between our calculations and our experimental data. We use our numerical model to estimate the change in the effective mode volume  $V_{\text{eff}}$  (see Equation 6 in Methods) when increasing the number of layers from one to seven. For the monolayer we estimate  $V_{\text{eff}}$  to be  $900 \text{ nm}^3$ , while for the multilayer this number naturally increases to  $2100 \text{ nm}^3$  due to the seven times larger integration volume  $\mathcal{V}$ . This larger effective mode volumes means that a larger number of excitons can couple coherently with the plasmon field, thus increasing the overall cou-

pling strength. Note however, that relatively the effective mode volume calculated for each layer decreases significantly to an average value of  $390 \text{ nm}^3$ . This is caused by a higher permittivity of the environment experienced by each of the seven layers. A higher number of excitons involved in the coupling can explain the substantial change in the Rabi splitting observed experimentally between mono- and multilayers  $\text{WS}_2$ . This conclusion is in agreement with recent experimental works.<sup>25,30</sup>

## Conclusion

We have successfully demonstrated the onset of the strong-coupling regime between monolayer  $\text{WS}_2$  flakes and single-crystalline gold nanodisks with a Rabi splitting of  $108 \pm 8 \text{ meV}$ . The natural variation in the nanodisk radius allowed us to probe the coupled system around the exciton energy and map out the avoided crossing. Spurred by recent experiments, we furthermore demonstrated an even stronger coupling between the nanodisks and multilayer  $\text{WS}_2$  yielding a Rabi splitting of  $175 \pm 9 \text{ meV}$ , i.e. in excess of seven times  $k_B T$  at room temperature. This is enabled by a larger overlap of the plasmon mode and the increased number of excitons located in multilayer  $\text{WS}_2$ . This way of controlling the coupling regime in plasmonic nanodisks and structurally similar systems is a key component towards applications within all-optical circuitry, polaritonic lasers, and quantum information processing, as well as the exploration of possible anti-bunching effects in multi-emitters coupled to plasmonic cavities.<sup>13,58</sup>

## Methods

### Optical measurements

A custom spectroscopy setup built from a Nikon Eclipse Ti-U inverted microscope was used for the optical measurements. For the dark-field and bright-field spectra a halogen lamp with a tunable power up to 100 W was used, while for the photoluminescence a 407 nm diode laser (Integrated Optics) was used. The light was

focused on the sample with a TU Plan Fluor objective from Nikon (100 $\times$ , 0.9 NA) and collected with the same objective. Afterwards, the light was directed toward a slit allowing for precise selection of the collection area. The light then entered a Shamrock 303i Spectrometer equipped with a 450 nm longpass filter (FELH0450 from Thorlabs) and an electronically cooled Newton 970 EMCCD for acquiring spectra. All spectra consist of the sum of several lines on the 2D CCD uniquely identified for each particle. Each of these spectra were first corrected for dark counts, and then for background using the local environment in close vicinity of the individual particles obtained directly from the same spectroscopic image. Finally, the spectra were divided by the normalized white light spectrum of the halogen lamp. The photoluminescence spectra were obtained in a similar manner apart from the white light spectrum correction. All experiments were performed at room temperature.

## Finite-element calculations

A commercially available FEM software (COMSOL Multiphysics v. 5.3a) was used to simulate the electrodynamic response of the nanodisks placed on top of mono- and multilayer WS<sub>2</sub>. We used experimental measurements of the nanoparticles to estimate their radii, which gave us nanodisks with radii ranging from 19 nm to 29 nm for our calculations on monolayer WS<sub>2</sub>. Due to higher values of the dielectric function and a higher thickness of the multilayers WS<sub>2</sub>, the LSPR of the nanodisks were redshifted and the radii close to the excitonic resonance ranged from 11 nm to 21 nm. In all our calculations, we have used a thickness of 9 nm for the metallic core.<sup>37</sup> For this we used the dielectric function measured by McPeak et al.<sup>52</sup> to better reflect the single-crystalline nature of our nanoparticles. We model the layer of CTAB molecule as a homogeneous 1 nm thick dielectric layer surrounding the nanodisks with a refractive index of 1.435.<sup>59</sup> The nanodisk with the CTAB layer is in direct contact with WS<sub>2</sub>. The one and seven layers WS<sub>2</sub> are modelled as homogeneous, isotropic bulk materials with thicknesses

of 0.6 nm and 4.3 nm, respectively, and the dielectric functions for both cases are extracted from experimental reflection measurements followed by a treatment with the transfer-matrix method (see Table S1 and S2). The SiO<sub>2</sub> substrate is modelled as a semi-infinite layer and the dielectric function is taken from Malitson.<sup>60</sup> The exciting field is impinging at normal incidence onto the nanodisk. The scattering cross section is evaluated by integrating the scattered energy density flow through a surface with a radius of 100 nm placed 150 nm above the nanodisk to simulate the numerical aperture of the objective used in our measurements (see optical measurements section above). The absorption cross section is calculated by integrating the energy density dissipated within the volume of the metallic core of the nanodisk and within the layered material WS<sub>2</sub> located below the nanodisk. The mesh size inside the WS<sub>2</sub> layers, the CTAB layer and in the metal core close to the metal/CTAB interface is as small as 0.3 nm to allow numerical convergence. The rest of the core of the nanodisk is meshed with elements with sizes ranging from 0.3 nm to 4 nm. For the effective mode volume calculations (see section below), we calculate Equation 6 within a volume  $\mathcal{V}$  inside WS<sub>2</sub> (taking into account the spectral dispersion) and restricted within a radius of 50 nm around the nanodisks. In the special case of the seven-layer WS<sub>2</sub>, we calculate the effective mode volume  $V_{\text{eff}}$  for each of the seven layers.

## Effective mode volume calculations

In cavity quantum-electrodynamics (QED), the mode volume  $V$  associated with a single exciton in the point  $\mathbf{r}_0$  is commonly given by<sup>61</sup>

$$V = \frac{\sum_{\alpha=x,y,z} \int d\mathbf{r} \epsilon(\mathbf{r}) |E_{\alpha}(\mathbf{r})|^2}{\sum_{\alpha=x,y,z} \epsilon(\mathbf{r}_0) |E_{\alpha}(\mathbf{r}_0)|^2}, \quad (5)$$

where the electrical field  $\mathbf{E}$  is evaluated at the exciton frequency, and with the integral over the energy density extending over all space. The energy density can be appropriately corrected to account for dispersive media, such as metallic elements.<sup>61</sup> The lower part of the frac-

tion contains the field enhancement at the position of the exciton, including an implicit average over all possible dipole directions.

To account for multiple excitons distributed in a quasi 2D layer, we calculate the effective mode volume  $V_{\text{eff}}$  following the prescription by Wen et al.<sup>29</sup> as

$$V_{\text{eff}} = \frac{\sum_{\alpha=x,y} \int_{\mathcal{V}} d\mathbf{r} \epsilon(\mathbf{r}) |E_{\alpha}(\mathbf{r})|^2}{\sum_{\alpha=x,y} \epsilon(\mathbf{r}_0) |E_{\alpha}(\mathbf{r}_0)|^2}, \quad (6)$$

where  $\mathbf{r}_0$  is now located within  $\mathcal{V}$ , and  $\epsilon$  is the dielectric function of the layered 2D material (in the absence of the exciton transition). Perhaps intuitively, the spatial integral over the energy density is restricted to the volume  $\mathcal{V}$  of the layered 2D material, including only in-plane field components  $E_x$  and  $E_y$  in accordance with the in-plane orientation of the dipole moments of the 2D excitons. We emphasize that this expression can be substantiated through rigorous summation of spatially uniformly distributed dipoles within the volume  $\mathcal{V}$  of the layered 2D material, while subsequently accommodating an effective number ( $N_{\text{eff}}$ ) of dipoles in the point  $\mathbf{r}_0$ , eventually causing the same effective coupling constant  $g \propto \sqrt{N_{\text{eff}}/V_{\text{eff}}}$ . As a result,  $N_{\text{eff}} = \rho \times V_{\text{eff}}$ , where  $\rho$  is the volume density of dipoles throughout the homogeneous layered 2D material.

## Acknowledgments

We thank C. Tserkezis and J. M. Hvam for stimulating discussions. The Center for Nanostructured Graphene is sponsored by the Danish National Research Foundation (Project No. DNRF103). F. T. acknowledges a MULTIPLY fellowship under the Marie Skłodowska-Curie COFUND Action (Grant Agreement No. 713694) N. A. M. is a VILLUM Investigator supported by VILLUM FONDEN (Grant No. 16498). T. R. and A. B. acknowledge the IDUN Center of Excellence funded by the Danish National Research Foundation (Project No. DNRF122) and VILLUM FONDEN (Grant No. 9301).

## References

- (1) Yoshie, T.; Scherer, A.; Hendrickson, J.; Khitrova, G.; Gibbs, H. M.; Rupper, G.; Ell, C.; Shchekin, O. B.; Deppe, D. G. Vacuum Rabi splitting with a single quantum dot in a photonic crystal nanocavity. *Nature* **2004**, *432*, 200–203.
- (2) Wallraff, A.; Schuster, D. I.; Blais, A.; Frunzio, L.; Huang, R.-S.; Majer, J.; Kumar, S.; Girvin, S. M.; Schoelkopf, R. J. Strong coupling of a single photon to a superconducting qubit using circuit quantum electrodynamics. *Nature* **2004**, *431*, 162–167.
- (3) McKeever, J.; Boca, A.; Boozer, A. D.; Buck, J. R.; Kimble, H. J. Experimental realization of a one-atom laser in the regime of strong coupling. *Nature* **2003**, *425*, 268–271.
- (4) Marcos, D.; Wubs, M.; Taylor, J. M.; Aguado, R.; Lukin, M. D.; Sørensen, A. S. Coupling Nitrogen-Vacancy Centers in Diamond to Superconducting Flux Qubits. *Phys. Rev. Lett.* **2010**, *105*, 210501.
- (5) Zhu, X.; Saito, S.; Kemp, A.; Kakuyanagi, K.; Karimoto, S.-i.; Nakano, H.; Munro, W. J.; Tokura, Y.; Everitt, M. S.; Nemoto, K.; Kasu, M.; Mizuochi, N.; Semba, K. Coherent coupling of a superconducting flux qubit to an electron spin ensemble in diamond. *Nature* **2011**, *478*, 221–224.
- (6) Todisco, F.; De Giorgi, M.; Esposito, M.; De Marco, L.; Zizzari, A.; Bianco, M.; Dominici, L.; Ballarini, D.; Arima, V.; Gigli, G.; Sanvitto, D. Ultrastrong Plasmon-Exciton Coupling by Dynamic Molecular Aggregation. *ACS Photonics* **2018**, *5*, 143–150.
- (7) Kamandar Dezfouli, M.; Tserkezis, C.; Mortensen, N. A.; Hughes, S. Nonlocal quasinormal modes for arbitrarily shaped three-dimensional plasmonic resonators. *Optica* **2017**, *4*, 1503.

- (8) Törmä, P.; Barnes, W. L. Strong coupling between surface plasmon polaritons and emitters: a review. *Rep. Prog. Phys.* **2015**, *78*, 013901.
- (9) Marquier, F.; Sauvan, C.; Greffet, J.-J. Revisiting Quantum Optics with Surface Plasmons and Plasmonic Resonators. *ACS Photonics* **2017**, *4*, 2091–2101.
- (10) Baranov, D. G.; Wersäll, M.; Cuadra, J.; Antosiewicz, T. J.; Shegai, T. Novel Nanostructures and Materials for Strong Light-Matter Interactions. *ACS Photonics* **2018**, *5*, 24–42.
- (11) Vasa, P.; Lienau, C. Strong Light-Matter Interaction in Quantum Emitter/Metal Hybrid Nanostructures. *ACS Photonics* **2018**, *5*, 2–23.
- (12) Gonçalves, P. A. D.; Bertelsen, L. P.; Xiao, S.; Mortensen, N. A. Plasmon-exciton polaritons in two-dimensional semiconductor/metal interfaces. *Phys. Rev. B* **2018**, *97*, 041402(R).
- (13) Fernández-Domínguez, A. I.; Bozhevolnyi, S. I.; Mortensen, N. A. Plasmon-Enhanced Generation of Nonclassical Light. *ACS Photonics* **2018**, *5*, 3447–3451.
- (14) Berrier, A.; Cools, R.; Arnold, C.; Offermans, P.; Crego-Calama, M.; Brongersma, S. H.; Gómez-Rivas, J. Active Control of the Strong Coupling Regime between Porphyrin Excitons and Surface Plasmon Polaritons. *ACS Nano* **2011**, *5*, 6226–6232.
- (15) Zengin, G.; Wersäll, M.; Nilsson, S.; Antosiewicz, T. J.; Käll, M.; Shegai, T. Realizing Strong Light-Matter Interactions between Single-Nanoparticle Plasmons and Molecular Excitons at Ambient Conditions. *Phys. Rev. Lett.* **2015**, *114*, 157401.
- (16) Chikkaraddy, R.; de Nijs, B.; Benz, F.; Barrow, S. J.; Scherman, O. A.; Rosta, E.; Demetriadou, A.; Fox, P.; Hess, O.; Baumberg, J. J. Single-molecule strong coupling at room temperature in plasmonic nanocavities. *Nature* **2016**, *535*, 127–130.
- (17) Wersäll, M.; Cuadra, J.; Antosiewicz, T. J.; Balci, S.; Shegai, T. Observation of Mode Splitting in Photoluminescence of Individual Plasmonic Nanoparticles Strongly Coupled to Molecular Excitons. *Nano Lett.* **2017**, *17*, 551–558.
- (18) Ramezani, M.; Halpin, A.; Fernández-Domínguez, A. I.; Feist, J.; Rodriguez, S. R.-K.; Garcia-Vidal, F. J.; Gómez Rivas, J. Plasmon-exciton-polariton lasing. *Optica* **2017**, *4*, 31.
- (19) De Giorgi, M.; Ramezani, M.; Todisco, F.; Halpin, A.; Caputo, D.; Fieramosca, A.; Gomez-Rivas, J.; Sanvitto, D. Interaction and Coherence of a Plasmon-Exciton Polariton Condensate. *ACS Photonics* **2018**, *5*, 3666–3672.
- (20) Liu, W.; Lee, B.; Naylor, C. H.; Ee, H.-S.; Park, J.; Johnson, A. T. C.; Agarwal, R. Strong Exciton-Plasmon Coupling in MoS<sub>2</sub> Coupled with Plasmonic Lattice. *Nano Lett.* **2016**, *16*, 1262–1269.
- (21) Wang, S.; Li, S.; Chervy, T.; Shalabney, A.; Azzini, S.; Orgiu, E.; Hutchison, J. A.; Genet, C.; Samorì, P.; Ebbesen, T. W. Coherent Coupling of WS<sub>2</sub> Monolayers with Metallic Photonic Nanostructures at Room Temperature. *Nano Lett.* **2016**, *16*, 4368–4374.
- (22) Liu, X.; Galfsky, T.; Sun, Z.; Xia, F.; Lin, E.-c.; Lee, Y.-H.; Kéna-Cohen, S.; Menon, V. M. Strong light-matter coupling in two-dimensional atomic crystals. *Nat. Photon.* **2015**, *9*, 30–34.
- (23) Flatten, L. C.; He, Z.; Coles, D. M.; Trichet, A. A. P.; Powell, A. W.; Taylor, R. A.; Warner, J. H.; Smith, J. M. Room-temperature exciton-polaritons with two-dimensional WS<sub>2</sub>. *Sci. Rep.* **2016**, *6*, 33134.

- (24) Hu, T.; Wang, Y.; Wu, L.; Zhang, L.; Shan, Y.; Lu, J.; Wang, J.; Luo, S.; Zhang, Z.; Liao, L.; Wu, S.; Shen, X.; Chen, Z. Strong coupling between Tamm plasmon polariton and two dimensional semiconductor excitons. *Appl. Phys. Lett.* **2017**, *110*, 051101.
- (25) Kleemann, M.-E.; Chikkaraddy, R.; Alexeev, E. M.; Kos, D.; Carnegie, C.; Deacon, W.; de Pury, A. C.; Große, C.; de Nijs, B.; Mertens, J.; Tartakovskii, A. I.; Baumberg, J. J. Strong-coupling of WSe<sub>2</sub> in ultra-compact plasmonic nanocavities at room temperature. *Nat. Commun.* **2017**, *8*, 1296.
- (26) Han, X.; Wang, K.; Xing, X.; Wang, M.; Lu, P. Rabi Splitting in a Plasmonic Nanocavity Coupled to a WS<sub>2</sub> Monolayer at Room Temperature. *ACS Photonics* **2018**, *5*, 3970–3976.
- (27) Tserkezis, C.; Gonçalves, P. A. D.; Wolff, C.; Todisco, F.; Busch, K.; Mortensen, N. A. Mie excitons: Understanding strong coupling in dielectric nanoparticles. *Phys. Rev. B* **2018**, *98*, 155439.
- (28) Groß, H.; Hamm, J. M.; Tufarelli, T.; Hess, O.; Hecht, B. Near-field strong coupling of single quantum dots. *Sci. Adv.* **2018**, *4*, eaar4906.
- (29) Wen, J.; Wang, H.; Wang, W.; Deng, Z.; Zhuang, C.; Zhang, Y.; Liu, F.; She, J.; Chen, J.; Chen, H.; Deng, S.; Xu, N. Room-Temperature Strong Light-Matter Interaction with Active Control in Single Plasmonic Nanorod Coupled with Two-Dimensional Atomic Crystals. *Nano Lett.* **2017**, *17*, 4689–4697.
- (30) Stührenberg, M.; Munkhbat, B.; Baranov, D. G.; Cuadra, J.; Yankovich, A. B.; Antosiewicz, T. J.; Olsson, E.; Shegai, T. Strong Light-Matter Coupling between Plasmons in Individual Gold Bi-pyramids and Excitons in Mono- and Multilayer WSe<sub>2</sub>. *Nano Lett.* **2018**, *18*, 5938–5945.
- (31) Cuadra, J.; Baranov, D. G.; Wersäll, M.; Verre, R.; Antosiewicz, T. J.; Shegai, T. Observation of Tunable Charged Exciton Polaritons in Hybrid Monolayer WS<sub>2</sub>-Plasmonic Nanoantenna System. *Nano Lett.* **2018**, *18*, 1777–1785.
- (32) Wang, Q.; Sun, L.; Zhang, B.; Chen, C.; Shen, X.; Lu, W. Direct observation of strong light-exciton coupling in thin WS<sub>2</sub> flakes. *Opt. Express* **2016**, *24*, 7151.
- (33) Yadgarov, L.; Višić, B.; Abir, T.; Tenne, R.; Polyakov, A. Y.; Levi, R.; Dolgova, T. V.; Zubyuk, V. V.; Fedyanin, A. A.; Goodilin, E. A.; Ellenbogen, T.; Tenne, R.; Oron, D. Strong light-matter interaction in tungsten disulfide nanotubes. *Phys. Chem. Chem. Phys.* **2018**, *20*, 20812–20820.
- (34) Munkhbat, B.; Baranov, D. G.; Stührenberg, M.; Wersäll, M.; Bisht, A.; Shegai, T. Self-hybridized exciton-polaritons in multilayers of transition metal dichalcogenides for efficient light absorption. *ACS Photonics* **2018**, doi: 10.1021/acsp Photonics.8b01194.
- (35) Gong, S.-H.; Alpeggiani, F.; Sciacca, B.; Garnett, E. C.; Kuipers, L. Nanoscale chiral valley-photon interface through optical spin-orbit coupling. *Science* **2018**, *359*, 443–447.
- (36) Chervy, T.; Azzini, S.; Lorchat, E.; Wang, S.; Gorodetski, Y.; Hutchinson, J. A.; Berciaud, S.; Ebbesen, T. W.; Genet, C. Room Temperature Chiral Coupling of Valley Excitons with Spin-Momentum Locked Surface Plasmons. *ACS Photonics* **2018**, *5*, 1281–1287.
- (37) Cui, X.; Qin, F.; Ruan, Q.; Zhuo, X.; Wang, J. Circular Gold Nanodisks with Synthetically Tunable Diameters and Thicknesses. *Adv. Funct. Mater.* **2018**, *28*, 1705516.

- (38) Gutiérrez, H. R.; Perea-López, N.; Elías, A. L.; Berkdemir, A.; Wang, B.; Lv, R.; López-Urías, F.; Crespi, V. H.; Terrones, H.; Terrones, M. Extraordinary Room-Temperature Photoluminescence in Triangular WS<sub>2</sub> Monolayers. *Nano Lett.* **2013**, *13*, 3447–3454.
- (39) Schuller, J. A.; Karaveli, S.; Schiros, T.; He, K.; Yang, S.; Kymissis, I.; Shan, J.; Zia, R. Orientation of luminescent excitons in layered nanomaterials. *Nat. Nanotechnol.* **2013**, *8*, 271–276.
- (40) Ramasubramaniam, A. Large excitonic effects in monolayers of molybdenum and tungsten dichalcogenides. *Phys. Rev. B* **2012**, *86*, 115409.
- (41) Jessen, B. S.; Whelan, P. R.; Mackenzie, D. M. A.; Luo, B.; Thomsen, J. D.; Gammelgaard, L.; Booth, T. J.; Bøggild, P. Quantitative optical mapping of two-dimensional materials. *Sci. Rep.* **2018**, *8*, 6381.
- (42) Christiansen, D.; Selig, M.; Berghäuser, G.; Schmidt, R.; Niehues, I.; Schneider, R.; Arora, A.; de Vasconcelos, S. M.; Bratschitsch, R.; Malic, E.; Knorr, A. Phonon Sidebands in Monolayer Transition Metal Dichalcogenides. *Phys. Rev. Lett.* **2017**, *119*, 187402.
- (43) Currie, M.; Hanbicki, A. T.; Kioseoglou, G.; Jonker, B. T. Optical control of charged exciton states in tungsten disulfide. *Appl. Phys. Lett.* **2015**, *106*, 201907.
- (44) Zhan, T.; Shi, X.; Dai, Y.; Liu, X.; Zi, J. Transfer matrix method for optics in graphene layers. *J. Phys. Condens. Matter* **2013**, *25*, 215301.
- (45) Qin, F.; Zhao, T.; Jiang, R.; Jiang, N.; Ruan, Q.; Wang, J.; Sun, L.-D.; Yan, C.-H.; Lin, H.-Q. Thickness Control Produces Gold Nanoplates with Their Plasmon in the Visible and Near-Infrared Regions. *Adv. Opt. Mater.* **2016**, *4*, 76–85.
- (46) Wang, F.; Shen, Y. R. General Properties of Local Plasmons in Metal Nanostructures. *Phys. Rev. Lett.* **2006**, *97*, 206806.
- (47) Flick, J.; Rivera, N.; Narang, P. Strong light-matter coupling in quantum chemistry and quantum photonics. *Nanophotonics* **2018**, *7*, 1479–1501.
- (48) Wu, X.; Gray, S. K.; Pelton, M. Quantum-dot-induced transparency in a nanoscale plasmonic resonator. *Opt. Express* **2010**, *18*, 23633.
- (49) Cong, C.; Shang, J.; Wang, Y.; Yu, T. Optical Properties of 2D Semiconductor WS<sub>2</sub>. *Adv. Opt. Mater.* **2018**, *6*, 1700767.
- (50) Antosiewicz, T. J.; Apell, S. P.; Shegai, T. Plasmon-Exciton Interactions in a Core-Shell Geometry: From Enhanced Absorption to Strong Coupling. *ACS Photonics* **2014**, *1*, 454–463.
- (51) Yorulmaz, M.; Nizzero, S.; Hoggard, A.; Wang, L.-Y.; Cai, Y.-Y.; Su, M.-N.; Chang, W.-S.; Link, S. Single-Particle Absorption Spectroscopy by Photothermal Contrast. *Nano Lett.* **2015**, *15*, 3041–3047.
- (52) McPeak, K. M.; Jayanti, S. V.; Kress, S. J. P.; Meyer, S.; Iotti, S.; Rossinelli, A.; Norris, D. J. Plasmonic Films Can Easily Be Better: Rules and Recipes. *ACS Photonics* **2015**, *2*, 326–333.
- (53) Olmon, R. L.; Slovick, B.; Johnson, T. W.; Shelton, D.; Oh, S.-H.; Boreman, G. D.; Raschke, M. B. Optical dielectric function of gold. *Phys. Rev. B* **2012**, *86*, 235147.
- (54) Johnson, P. B.; Christy, R. W. Optical Constants of the Noble Metals. *Phys. Rev. B* **1972**, *6*, 4370–4379.
- (55) Yakubovsky, D. I.; Arsenin, A. V.; Stebunov, Y. V.; Fedyanin, D. Y.; Volkov, V. S. Optical constants and structural properties of thin gold films. *Opt. Express* **2017**, *25*, 25574.

- (56) Zheng, D.; Zhang, S.; Deng, Q.; Kang, M.; Nordlander, P.; Xu, H. Manipulating Coherent Plasmon-Exciton Interaction in a Single Silver Nanorod on Monolayer WSe<sub>2</sub>. *Nano Lett.* **2017**, *17*, 3809–3814.
- (57) Bisht, A.; Cuadra, J.; Wersäll, M.; Canales, A.; Antosiewicz, T. J.; Shegai, T. Collective Strong Light-Matter Coupling in Hierarchical Microcavity-Plasmon-Exciton Systems. *Nano Lett.* **2018**, doi: 10.1021/acs.nanolett.8b03639.
- (58) Sáez-Blázquez, R.; Feist, J.; Fernández-Domínguez, A. I.; García-Vidal, F. J. Enhancing photon correlations through plasmonic strong coupling. *Optica* **2017**, *4*, 1363.
- (59) Kekicheff, P.; Spalla, O. Refractive Index of Thin Aqueous Films Confined between Two Hydrophobic Surfaces. *Langmuir* **1994**, *10*, 1584–1591.
- (60) Malitson, I. H. Interspecimen Comparison of the Refractive Index of Fused Silica. *J. Opt. Soc. Am.* **1965**, *55*, 1205.
- (61) Koenderink, A. F. On the use of Purcell factors for plasmon antennas. *Opt. Lett.* **2010**, *35*, 4208.